USGS
science for a changing world

S-Wave Normal Mode Propagation in Aluminum Cylinders

Scientific Investigations Report 2010–5013

U.S. Department of the Interior
U.S. Geological Survey

S-Wave Normal Mode Propagation in Aluminum Cylinders

By Myung W. Lee and William F. Waite

Scientific Investigations Report 2010–5013

U.S. Department of the Interior
U.S. Geological Survey

U.S. Department of the Interior
KEN SALAZAR, Secretary

U.S. Geological Survey
Marcia K. McNutt, Director

U.S. Geological Survey, Reston, Virginia: 2010

Suggested citation:
Lee, M.W., and Waite, W. F., 2010, S-wave normal mode propagation in aluminum cylinders: U.S. Geological Survey Scientific Investigations Report 2010–5013, 18 p.

Contents

Figures

S-Wave Normal Mode Propagation in Aluminum Cylinders

By Myung W. Lee and William F. Waite

Abstract

Large amplitude waveform features have been identified in pulse-transmission shear-wave measurements through cylinders that are long relative to the acoustic wavelength. The arrival times and amplitudes of these features do not follow the predicted behavior of well-known bar waves, but instead they appear to propagate with group velocities that increase as the waveform feature's dominant frequency increases. To identify these anomalous features, the wave equation is solved in a cylindrical coordinate system using an infinitely long cylinder with a free surface boundary condition. The solution indicates that large amplitude normal-mode propagations exist. Using the high-frequency approximation of the Bessel function, an approximate dispersion relation is derived. The predicted amplitude and group velocities using the approximate dispersion relation qualitatively agree with measured values at high frequencies, but the exact dispersion relation should be used to analyze normal modes for full ranges of frequency of interest, particularly at lower frequencies.

Introduction

The transmission of shear waves through soil is strongly influenced by the stiffness of the intergranular contacts (Santamarina and others, 2001). Crystalline solids, such as ice or gas hydrate, forming in the pore spaces of an unconsolidated sediment can stiffen the intergranular contacts by cementing grains together or by forming as load-bearing components of the sediment (Sloan and Koh, 2007). Particularly in the case of methane gas hydrate, acoustic measurements have been used to quantify the pore-space saturation of this naturally occurring hydrate in marine and beneath permafrost sediments (for example, Dai and others, 2008; Helgerud and others, 1999; Lee and Collett, 2005). To calibrate the relation between the pore-space hydrate saturation and the acoustic wave velocity, laboratory wave-velocity tests have been conducted on granular samples containing known hydrate saturations (Berge and others, 1999; Waite and others, 2004; Priest and others, 2005; Yun and others, 2005).

When the sample length is long compared to the acoustic wavelength, the appearance of multiple, large-amplitude waveform features can obscure the shear wave arrival. This phenomenon first becomes apparent while making measurements using the gas hydrate and sediment test laboratory instrument (GHASTLI) (Winters and others, 2000). Because GHASTLI was designed for making triaxial measurements of soil strength, cylindrical samples with lengths 2–2.5 times greater than their diameters are required (American Society for Testing and Materials, 2003). Because of the large sample lengths required for use with GHASTLI, Waite and others first encountered these large-amplitude waveform features during their investigation in 2008 and determined that they typically occur when the sample diameter was approximately 10 times longer than the shear wave wavelength (Waite and others, 2008).

To identify these features and distinguish between the geometric and porous media controls on waveform features, a series of acoustic measurements on aluminum cylinders of varying length and diameter were carried out. Kolsky (1963) and Graff (1975) have extensively analyzed wave propagation in thin cylinders, but their low-frequency, bar-wave formulations are not appropriate for the high-frequency measurements discussed here. Based on the relationship between the velocity, frequency, and amplitude of the waveform features, we propose to identify the features using a normal mode at high frequency.

Normal mode solutions have been extensively investigated in the context of layered Earth models (Ewing and others, 1957; Brekhovskikh, 1960; Aki and Richards, 1980). Thurston (1978) reviewed the wave propagations in rods and clad rods using various normal mode solutions such as extensional and flexural modes. Recently, the normal mode solution in a cylindrical coordinate system applicable to measurements made in GHASTLI at frequencies in the megahertz range has been presented in Lee and Waite (2009). In Lee and Waite (2009), the analysis focused on the P-wave normal mode propagation using an approximated dispersion relationship appropriate for high frequencies. This report extends the theory developed by Lee and Waite (2009) to analyze anomalous shear waveforms.

Measuring Waveforms in Aluminum Cylinders

In GHASTLI, compressional- and shear-wave acoustic waveforms are generated and measured using piezo-electric transducer crystals, hereafter referred to as "crystals," mounted in cylindrical titanium endcaps (fig. 1*A*). Each endcap contains an axially-positioned, disk-shaped shear-wave (S-wave) crystal. The compressional-wave (P-wave) crystal, which measures the waveform's axial displacements, is an annular ring surrounding the S-wave crystal (fig. 1*B*) that measures radial displacements. The crystals are epoxied to the back of a 6.35-mm-thick titanium wear plate, the front of which is coupled to the aluminum cylinder with Panametrics shear wave couplant. For this discussion, only waveforms generated and received by the S-wave crystals are considered here. The P-waveforms are presented and discussed in Lee and Waite (2009).

A Panametrics Model 5800 Pulser-Receiver generates the 50-volt pulse used to excite the P- or S-crystal in one endcap. The pulse traverses the sample, is received by the S-crystal in the second endcap, is displayed on a Tektronix TDS-340 oscilloscope, and is stored to disk. For a given pair of S-crystals, the waveform is essentially independent of which crystal is the signal transmitter and which is the receiver. For the purpose of deriving a tractable mathematical model of this system, the S-wave signals are assumed to be generated from a point source on the cylindrical axis, with their radial motion measured across the full diameter of the receiving crystal.

Measured waveform arrival times contain a system delay time that depends on the wiring configuration, endcap, and crystal pair. This delay, which is the time required for a signal to propagate through the electronics, crystals, and endcap wear plates, must be subtracted from the measured arrival times before dividing by the sample length to obtain the velocity of a given waveform feature through the sample.

Waveforms were measured using two different endcap sets on 35-mm-diameter aluminum cylinders having three different lengths. Aluminum cylinders are designated as 100-, 150-, and 200-mm aluminum cylinders (actual lengths are 101.2952, 149.53, and 202.5523 mm), and the endcaps are denoted endcap set no. 1 and no. 2. Figure 2*A* shows waveforms measured using endcap set no. 1, for which two distinct arrivals with large, comparable amplitudes can be easily observed for each cylinder. In figure 2*A*, S100-1 and S100-2 represent the first and second large amplitude arrivals in a 100-mm aluminum cylinder, with corresponding labels given for the 150- and 200-mm cylinders.

Figure 3*A* shows the measured waveforms using endcap set no. 2, with S200-1 representing the first arrival feature with high-frequency content (blue), and S200-2 representing the low-frequency feature following S200-1 (red). In contrast to the measured waveforms shown in figure 2*A*, there are no distinct arrivals for these two waveform features in figure 3*A*, rather the high-frequency and low-frequency features make one continuous waveform. One marked difference between waveforms shown in figure 2*A* and figure 3*A* is the broader frequency content of the figure 3*A* waveforms.

Use of the normal mode theory derived below to identify features such as those shown in figures 2*A* and 3*A* requires the group velocity and dominant frequency of each feature. The group velocity is calculated from the feature's arrival time, accounting for the system delay time and sample length as discussed above. The dominant frequency is calculated from a spectral analysis of the waveform feature.

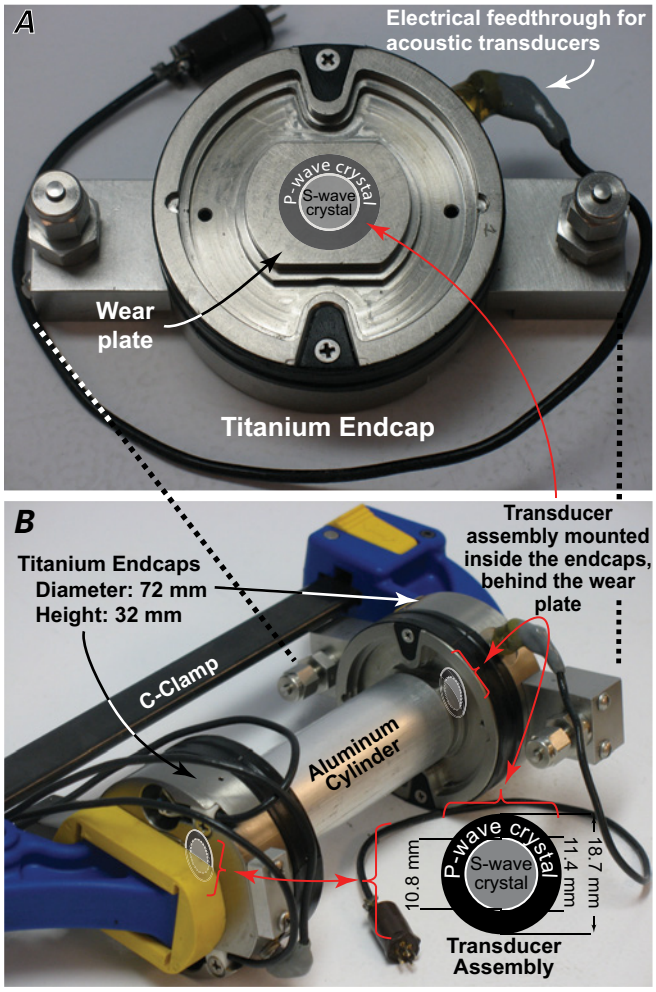

Figure 1. Measurement system. Within each endcap (*A*), the shear (S-wave) and compressional (P-wave) transducer crystals, shown schematically (*B*), are epoxied to the inner surface of a wear plate that contacts the sample. The 100-mm-long, 35-mm-diameter aluminum cylinder is shown here, with shear wave couplant between the aluminum and the end cap wear plates. A C-clamp holds the system together.

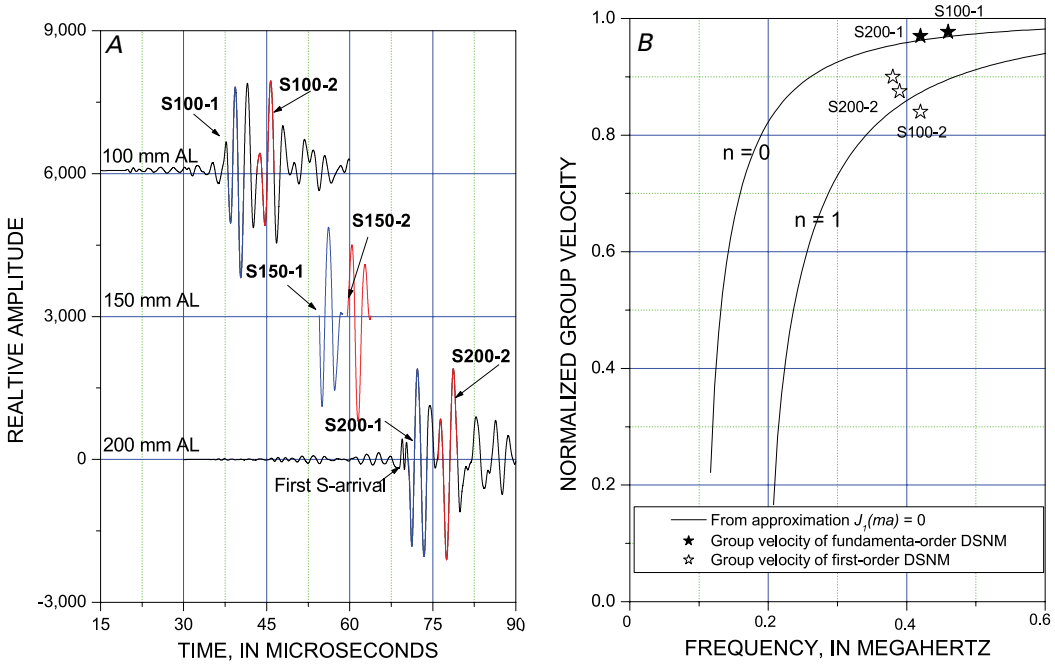

Figure 2. S-crystal waveforms and normalized group velocities measured using endcap set no. 1. *A*, Waveforms for 100-, 150-, and 200-mm-long aluminum cylinders. In the graph levels, the prefixes 100, 150, and 200 denote the length of the cylinder, and the suffixes 1 and 2 denote the first (blue) and second (red) large amplitude features, respectively. *B*, Measured normalized group velocities and approximated normalized group velocities derived from $J_1(ma) = 0$ with $n = 0$ and $n = 1$. DSNM, dispersive shear wave normal mode.

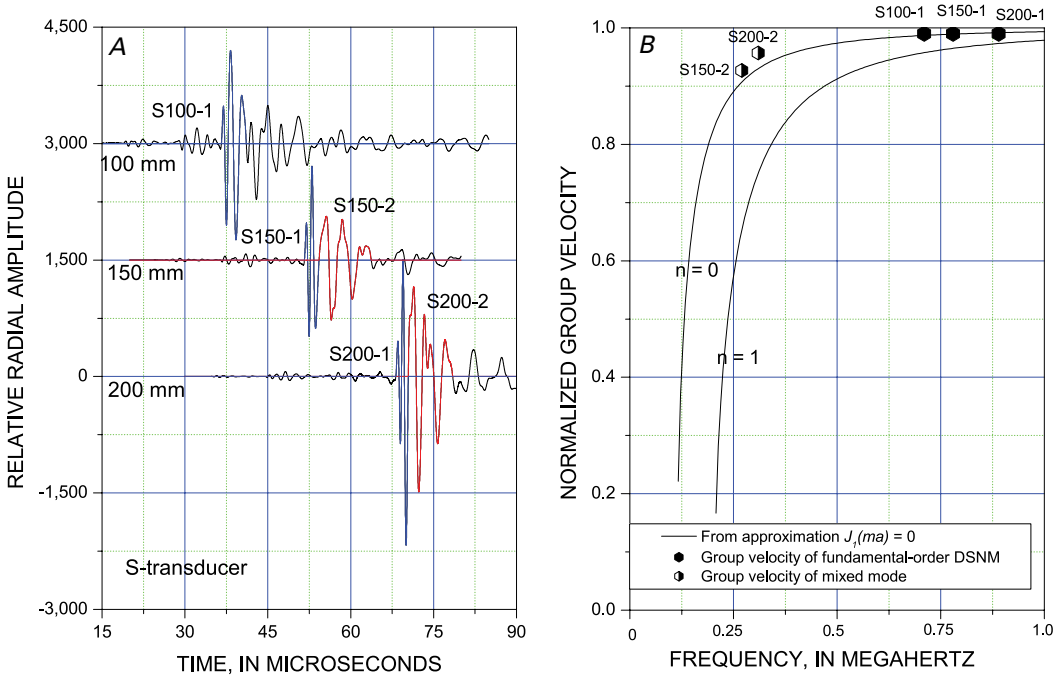

Figure 3. S-crystal waveforms and normalized group velocities measured using endcap set no. 2. *A*, Waveforms for 100-, 150-, and 200-mm-long aluminum cylinders. In the graph levels, the prefixes 100, 150, and 200 denote the length of the cylinder, and the suffixes 1 and 2 denote the first (blue) and second large amplitude features (red), respectively. *B*, Measured normalized group velocities and approximated normalized group velocities derived from $J_1(ma) = 0$ with $n = 0$ and $n = 1$. DSNM, dispersive shear wave normal mode.

Theory

Identifying the waveform features shown in figures 2*A* and 3*A* requires a theoretical relationship between each normal mode's dominant frequency and group velocity. We derive that relation in three steps:

1. Derive a solution of the wave propagation equation for cylinders.
2. Derive the dispersion relationship to obtain the normal mode phase velocity dependence on frequency.
3. Use the approximate or exact phase velocity at high frequency to calculate the group velocity for each normal mode.

As an additional check on the normal mode approach, we also derive the relative amplitudes of the normal modes as well as that of the S-body waves.

Solution of Wave Equation

Under the assumption of axial symmetry, differential equations for wave propagation inside an infinite cylinder in a cylindrical coordinate system (r,θ,z) can be written as:

$$\frac{\partial^2\Phi}{\partial r^2}+\frac{1}{r}\frac{\partial\Phi}{\partial r}+\frac{\partial^2\Phi}{\partial z^2}=\frac{1}{\alpha^2}\frac{\partial^2\Phi}{\partial^2 t}$$

$$\frac{\partial^2\Psi}{\partial r^2}+\frac{1}{r}\frac{\partial\Psi}{\partial r}-\frac{\Psi}{r^2}+\frac{\partial^2\Psi}{\partial z^2}=\frac{1}{\beta^2}\frac{\partial^2\Psi}{\partial^2 t} \qquad (1)$$

where Φ and Ψ are scalar potentials for P- and S-waves, respectively, and α, β, and t are P-wave velocity, S-wave velocity, and time, respectively (Biot, 1952; Lee and Balch, 1982). When the P-wave source is located at the origin with the strength of V_0 and the S-wave source is located at the origin with the strength of S_0, the formal solution of equation 1 in the frequency domain can be written as follows

$$\Phi=\int AJ_0(lr)e^{-ikz}dk+V_0\int H_0^{(2)}(lr)e^{-ikz}dk$$

$$\Psi=\int BJ_1(mr)e^{-ikz}dk+S_0\int H_1^{(2)}(mr)e^{-ikz}dk \qquad (2)$$

with

$$l=\left(\frac{\omega^2}{\alpha^2}-k^2\right)^{1/2} \qquad \text{for } \omega/\alpha > k,$$

$$l=-i\,\mathrm{sgn}\,\omega\left(k^2-\frac{\omega^2}{\alpha^2}\right) \qquad \text{for } \omega/\alpha < k,$$

$$m=\left(\frac{\omega^2}{\beta^2}-k^2\right)^{1/2} \qquad \text{for } \omega/\beta > k,$$

$$m=-i\,\mathrm{sgn}\,\omega\left(k^2-\frac{\omega^2}{\beta^2}\right) \qquad \text{for } \omega/\beta < k,$$

and

$$k=\omega/c$$

where ω is an angular frequency, c is the phase velocity, and J_n and $H_n^{(2)}$ are the Bessel functions of order n and the second kind Hankel function of order n, respectively, and A and B are constants to be determined by the boundary conditions. Note that uniformly expanding P- and S-wave sources are assumed for the wave equation solution.

The radial (U_r) and axial (U_z) displacement can be calculated by

$$U_r=\frac{\partial\Phi}{\partial r}-\frac{\partial\Psi}{\partial z} \quad \text{and} \quad U_z=\frac{\partial\Phi}{\partial z}+\frac{\partial\Psi}{\partial r}+\frac{\Psi}{r} \qquad (3)$$

In order to solve equation 1, two boundary conditions are utilized: vanishing radial stress, $p_{rr}=0$, and vanishing tangential stress, $p_{rz}=0$ at the cylinder surface. Stresses are given by:

$$p_{rr}=-\lambda\frac{\omega^2\Phi}{\alpha^2}+2\mu\left(\frac{\partial^2\Phi}{\partial r^2}-\frac{\partial^2\Psi}{\partial r\partial z}\right)$$

$$p_{rz}=\mu\left(2\frac{\partial^2\Phi}{\partial r\partial z}-\frac{\omega^2\Psi}{\beta^2}-2\frac{\partial^2\Psi}{\partial z^2}\right) \qquad (4)$$

where λ and μ are the Lamé parameters. Substituting these two boundary conditions into equation 3, the following matrix equation can be derived for a cylinder of radius a:

$$Q=\begin{bmatrix}a_{11} & a_{12}\\ a_{21} & a_{22}\end{bmatrix}\begin{bmatrix}A\\ B\end{bmatrix}=\begin{bmatrix}S_1\\ S_2\end{bmatrix} \qquad (5)$$

with

$$a_{11}=\rho(2k^2\beta^2-\omega^2)J_0(la)+2\rho\beta^2 lJ_1(la)/a,$$
$$a_{12}=2ik\mu[mJ_0(ma)-J_1(ma)/a],$$
$$a_{21}=i2k\mu lJ_1(la),$$
$$a_{22}=\rho(2k^2\beta^2-\omega^2)J_1(ma),$$
$$S_1=V_0\rho(\omega^2-2k^2\beta^2)H_0^{(2)}(la)-2V_0\rho\beta^2 lH_1^{(2)}(la)/a$$
$$-2ik\mu S_0[mH_0^2(ma)-H_1^{(2)}(ma)/a],$$

and

$$S_2=-V_0\mu 2iklH_1^{(2)}(la)-S_0\mu(2k^2-\omega^2/\beta^2)H_1^2(ma),$$

where ρ is the density of a cylinder.

Phase Velocity

The dispersion relation for the normal modes, which gives the phase velocity dependence on frequency, is given by setting the determinant of equation 5 equal to zero (Ewing and others, 1957). The determinant of matrix Q, Δ, is given by $a_{11}a_{22} - a_{12}a_{21}$:

$$\Delta = 4k^2\rho^2\beta^4 lJ_1(la)[mJ_0(ma) - J_1(ma)/a] + \rho^2(2k^2\beta^2 - \omega^2)J_1(ma)[(2k^2\beta^2 - \omega^2)J_0(la) + 2\beta^2 lJ_1(la)/a], \quad (6)$$

which agrees with Graff (1975). When the wave equation is solved using the dispersion relation derived from $\Delta = 0$, it is called the normal mode solution. The general solution is a superposition of each normal mode, with each normal mode having a unique phase velocity with respect to frequency. The dispersion relation for the dispersive S-wave normal mode (DSNM) is derived by requiring the phase velocity greater than the S-wave velocity and less than the P-wave velocity. In this case, l is purely imaginary and m is a real number. Although l is an imaginary number, there exist real values for k that solve equation 6. Equation 6 cannot be solved analytically, but the dispersion relationship can be numerically calculated following a similar method to that given for the P-wave normal modes by Lee and Waite (2009). The phase velocity of an S-wave normal mode (C_β) is given by $\Delta = 0$ and this can be written as:

$$\frac{\left(1 - \frac{2\beta^2}{C_\beta^2}\right)}{\frac{4\beta^3}{C_\beta^2\alpha}} = \frac{l^* J_1(la)\left[m^* J_0(ma) - \frac{\beta J_1(ma)}{a\omega}\right]}{J_1(ma)\left[\left(\frac{2\beta^2}{C_\beta^2} - 1\right)J_0(la) + \frac{2\beta^2 l^* J_1(la)}{a\alpha\omega}\right]} \quad (7)$$

where $l^* = \sqrt{1 - \alpha^2/C_\beta^2}$ and $m^* = \sqrt{1 - \beta^2/C_\beta^2}$.

Allowable phase velocities are those for which the left side of equation 7 is the same as the right side of equation 7 for a given phase velocity. As demonstrated in equation 7, the phase velocity of a given normal mode depends on the acoustic frequency, ω, the P- and S-wave velocities, α and β, and by the cylinder radius, a.

Figure 4*A* shows phase and group velocities, derived below, for the fundamental-order DSNM calculated for a 35-mm-diameter aluminum cylinder. As frequency increases, the phase velocity decreases continuously, reaching a minimum near 0.13 MHz. For frequencies greater than about 0.13 MHz, the phase velocity decreases monotonically with increasing frequency. The phase velocity discontinuity near

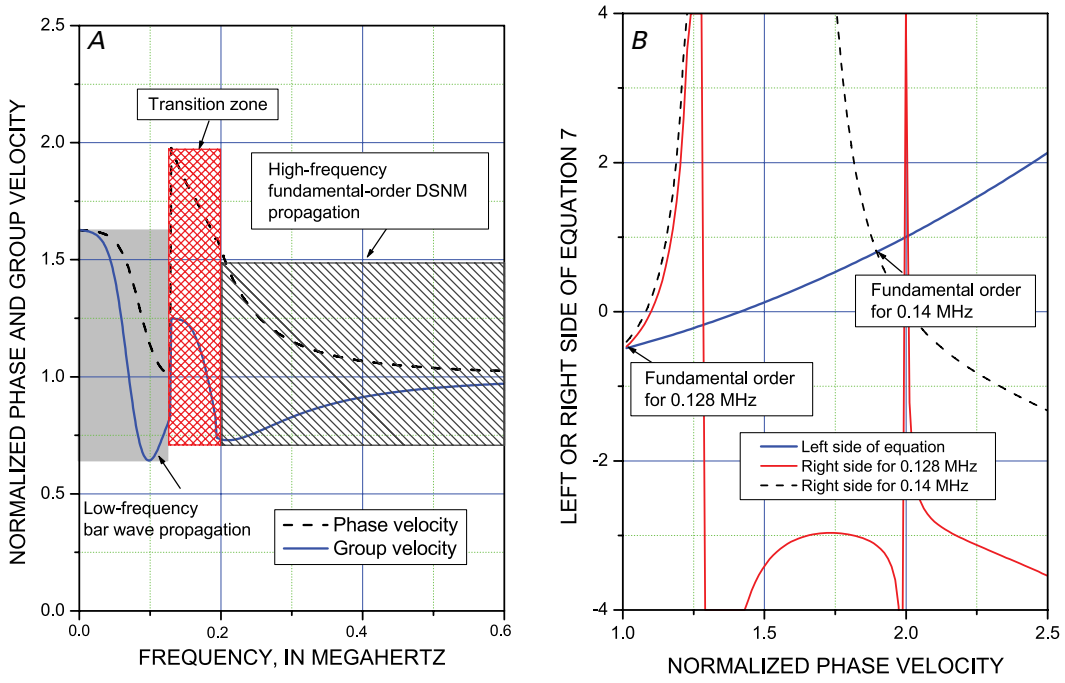

Figure 4. Normalized phase and group velocity. *A*, Numerically calculated phase and group velocities for the fundamental-order dispersive shear wave normal mode (DSNM) for an aluminum cylinder with a 35-mm diameter, P-wave velocity of 6,390 m/s and S-wave velocity of 3,180 m/s. *B*, Numerical solution of equation 7 showing phase velocities at 0.128 and 0.14 MHz.

0.13 MHz can be explained from figure 4*B*, where numerical solutions of phase velocities at two different frequencies just above and below 0.13 MHz are shown. The phase velocity of the fundamental order at 0.128 MHz is $C_\beta \approx \beta$, whereas the phase velocity at 0.14 MHz is $C_\beta \approx 2\beta$. The abrupt change of the phase velocity is not a numerical artifact, but instead marks the maximum frequency for bar wave propagation (indicated in fig. 4*A* by the shaded region).

The phase velocities at higher frequencies can be approximated using either $J_0(ma) = 0$ or $J_1(ma) = 0$. If the approximate solution $J_1(ma) = 0$ is used for the phase velocities, the DSNM phase velocity is given by the following equation by incorporating the high frequency approximation of the Bessel function $(J_1(ma) = \sqrt{2/(\pi am)}\cos(am - 3\pi/4)$; Watson, 1966):

$$C_\beta = \beta\sqrt{\frac{\omega^2 a^2}{\omega^2 a^2 - \beta^2 \Lambda_\beta^2}} \tag{8}$$

with $\Lambda_\beta = (5\pi/4 + n\pi)$ and $\Pi_\beta = a\omega/\beta$.

The approximate solution using $J_0(ma) = 0$ and its implication in the normal mode analysis is given in appendix 1.

When the phase velocity is less than the S-wave velocity, both *l* and *m* become imaginary. At high frequencies, the dispersion relationship can be written as

$$\frac{4mJ_1(la)J_0(ma)}{2 - C_\beta^2/\beta^2} = \frac{k^2(C_\beta^2/\beta^2 - 2)J_0(la)J_1(ma)}{l}. \tag{9}$$

Because $J_0(la)J_1(ma) \approx J_1(la)J_0(ma)$ as *l* and *m* become pure imaginary numbers, equation 9 becomes:

$$\frac{4\sqrt{1 - C_\beta^2/\beta^2}}{2 - C_\beta^2/\beta^2} = \frac{2 - C_\beta^2/\beta^2}{\sqrt{1 - C_\beta^2/\alpha^2}} \tag{10}$$

This is an identical form of Rayleigh wave dispersion relationship given in White (1965). In other words, a non-dispersive S-wave normal mode exists inside an aluminum cylinder if the wavelength is much smaller than the radius of the aluminum cylinder.

In this report, the normal mode's order is defined from $\Lambda_\beta = (5\pi/4 + n\pi)$. If the phase (or group) velocity of a waveform feature approximately agrees with equation 8 when $n = 0$, it is called the fundamental-order normal mode. If the phase (or group) velocity agrees with equation 8 when $n = 1$, it is called the first-order normal mode. This naming convention differs from that of Kolsky (1963) and Graff (1975). Their naming convention is based on the order of the numerical solution of the phase velocity (equation 7) in such a way that for a given frequency, the first solution (lowest phase velocity) is the first order and the second solution is the second order, and so forth.

Group Velocity

Group velocity (*G*) is given by Ewing and others (1957) as:

$$G = \frac{d\omega}{dk} = C + k\frac{dC}{dk} \tag{11}$$

Therefore, the S-wave normal mode group velocity (G_β) is:

$$G_\beta = \frac{d\omega}{dk} = \beta\sqrt{1 - \frac{\beta^2\Lambda_\beta^2}{a^2\omega^2}} = \beta\sqrt{1 - \frac{\Lambda_\beta^2}{\Pi_\beta^2}}. \tag{12}$$

Figure 4*A* also shows the numerically calculated group velocities using the exact dispersion relation for the fundamental-order DSNM. At higher frequencies greater than about 0.2 MHz, the group velocity is a monotonically increasing function of frequency. However, below 0.2 MHz there exists a local minimum group velocity near 0.1 MHz and a local maximum group velocity near 0.14 MHz. At near zero frequency, the phase and group velocities are equal and the group velocity is about $C_\beta \approx 1.63\beta$, the bar wave velocity shown in Kolsky (1963). Group velocities for frequencies up to 0.1 MHz follow the dispersion relation for the bar wave given in Kolsky (1963), which was derived from low frequency Bessel function approximations. The phase and group velocities approximated using equations 8 and 12 are valid for frequencies greater than about 0.4 MHz for this investigation, as shown later.

The low-frequency dispersion relation is different from that at high frequencies. For bar waves, which are governed by the low-frequency dispersion relation, the low-frequency component of wave feature arrives before the high-frequency component. For DSNM, which are governed by the high-frequency dispersion relation, the high-frequency component of wave feature arrives before the low-frequency component. Consequently, the bar wave and DSNM described in this paper have markedly different waveforms.

Amplitude

Amplitude relations provide an independent check on the normal mode interpretation for characterizing the waveform features shown in figures 2*A* and 3*A*. Relative amplitudes are also particularly useful when differentiating between the fundamental normal modes and the body waves used to determine S-wave speeds in materials. Normal mode amplitudes relative to each other can be calculated from equations 2 and 5. With P- and S-wave sources at the origin, the constants *A* and *B* in equations 2 and 5 are given by:

$$A = (S_1 a_{22} - S_2 a_{12})/\Delta \equiv \frac{A_p(k)}{\Delta(k)} \tag{13}$$

$$B = (-S_1 a_{21} + S_2 a_{11})/\Delta \equiv \frac{A_S(k)}{\Delta k}$$

In the following amplitude analysis, only the S-wave amplitude is considered. Then,

$$\begin{aligned} A_s(k) = {} & V_0(2k^2\beta^2 - \omega^2)2ik\rho^2\beta^2 l[J_1(la)H_0^{(2)}(la) \\ & - J_0(la)H_1^{(2)}(la)] \\ & + (V_0 4ik\rho^2\beta^4 l^2 J_1(la)H_1^{(2)}(la)/a) \\ & - S_0\rho^2\{4k^2\beta^4 l J_1(la)[mH_0^{(2)}(ma) - H_1^{(2)}(ma)/a] \\ & + (2k^2\beta^2 - \omega^2)^2 J_0(la)H_1^{(2)}(ma)\} \end{aligned} \tag{14}$$

Substituting B into the integral equation shown in equation 2, the potential for the S-wave solution is given by the following equation in the lower half of the complex k-plane (for example, Pekeris, 1948; Ewing and others, 1957; Båth, 1968):

$$\begin{aligned} \Psi(k) &= \int_{-\infty}^{\infty} B(k)J_1(mr)e^{-ikz}dk + S_0\int_{-\infty}^{\infty} H_1^{(2)}(mr)e^{-ikz}dk \\ &= \int_{Branch\ cut}[\boldsymbol{B}(k)J_1(mr) + S_0H_1^{(2)}(mr)]e^{-ikz}dk - 2\pi i\sum R_n^S \\ &= \Psi_B + \Psi_{DSNM} \end{aligned} \tag{15}$$

where *Branch cut* is a branch cut integration around the branch points $k_\alpha = \omega/\alpha$ and $k_\beta = \omega/\beta$, R^S_n is the residue of integration for dispersive S-wave normal modes, and Ψ_B and Ψ_{DSNM} are S-wave potentials for body wave and dispersive S-wave normal modes, respectively.

Amplitude of the Dispersive S-Wave Normal Mode

The amplitude of the dispersive S-wave normal modes can be calculated by substituting solutions of the dispersion relation into equation 14. The solution for DSNM is given by

$$\Psi_{DSNM} = \frac{-2\pi i A_S(k)J_1(mr)e^{-ikz}}{\partial\Delta\partial k}\Big]\Big|_{k=solution\ of\ equation\ 6} \tag{16}$$

where Δ is given in equation 6 and $AS(k)$ is given in equation 14.

Amplitude of the Body Wave

The branch cut integrations shown in equation 15 yield body wave motions inside the solid. The branch cut integration can be evaluated using the steepest decent method if the observation point is in the far field, meaning the wave travels a distance much longer than its wavelength (for example, Morse and Feshbach, 1953; Båth, 1968; Greenfield, 1978). Using Hankel functions, equation 15 can be written as

$$\begin{aligned} \Psi(\omega) &= \int_{-\infty}^{\infty} B(k)J_1(mr)e^{-ikz}dk + S_0\int H_1^{(2)}(mr)e^{-ikz}dk \\ &= \frac{1}{2}\int_{-\infty}^{\infty}[B(k)H_1^{(1)}(mr) + (B(k) + 2S_0)H_1^{(2)}(mr)]e^{-ikz}dk. \end{aligned} \tag{17}$$

The integration using the steepest decent method yields

$$\Psi_B \approx \frac{-2B(k_\beta\cos\phi)\cos(\omega R/\beta)}{R} - \frac{2S_0e^{-i\omega R/\beta}}{R}$$

where $k_\beta = \omega/\beta$, $\phi = \tan^{-1}(r/z)$, and $R = \sqrt{z^2 + r^2}$.

The displacements can be written as:

$$\begin{aligned} U_z &= \frac{\partial\Psi_B}{\partial r} + \frac{\Psi_B}{r} \approx \\ & \frac{2\omega rB(k_\beta\cos\phi)\sin(\omega R/\beta)}{\beta R^2} - \frac{2i\omega rV_0e^{-i\omega R/\phi}}{\beta R^2} \\ & - \frac{2B(k_\beta\cos\phi)\cos(\omega R/\beta)}{rR} - \frac{2S_0e^{-i\omega R/\phi}}{rR} \end{aligned} \tag{18}$$

$$U_r = -\frac{\partial\Psi_B}{\partial z} \approx \frac{2\omega zB(k_\beta\cos\phi)\sin(\omega R/\beta)}{\beta R^2} - \frac{2i\omega zV_0e^{-i\omega R/\beta}}{\beta R^2}$$

The far-field solution shown in equation 17 requires that $mr >> 1$. The geometry of our measurement, however, does not satisfy this condition, because the cylinder radius, a, and hence, the observation point radius, r, are both small. The body wave amplitude can, therefore, only be approximated by assuming the uniformly expanding source waveform can be calculated by making a and r large. In other words, the first term of equation 17, because this term yields the reflections from the cylinder boundaries, can be ignored. From equation 17, the amplitude of S-wave body wave generated by a S-wave source can be approximated by:

$$\begin{aligned} U_r &= \frac{2i\omega S_0e^{-i\omega z/\beta}}{\beta z} \\ U_z &\approx 0 \end{aligned} \tag{19}$$

Because only shear waves generated by the S-wave source (S_0) were considered for the following amplitude analysis, V_0 can be set to zero in equation 14.

Theoretical amplitudes presented here are displacements of the particles and are proportional to the amplitudes of measured waveforms. Because we are only interested in comparing amplitude within a single waveform, the fact that displacement and amplitude are proportional means that they can be used interchangeably.

Analysis of Measured Waveforms

The waveform features shown in figure 2*A* are interpreted as the fundamental and first-order DSNM. For example, S150-1 is the fundamental-order DSNM and S150-2 is the first-order DSNM for the 150-mm aluminum cylinder. The measured group velocities of the fundamental and first-order DSNM for the 100-, 150-, and 200-mm aluminum cylinders are shown in figure 2*B* along with the calculated group velocities derived from $J_1(ma) = 0$ with $n = 0$ and $n = 1$. The arrival times of the fundamental-order DSNM and S-wave body wave are close, thus the waveforms shown as S100-1, S150-1, and S200-1 in figure 2*A* are mixtures of the body wave and DSNM. However, for the 200 mm-aluminum cylinder, the slightly faster body S-wave is able to separate from the fundamental-order normal mode and is observed as a small amplitude wave with high frequency content arriving earlier than S200-1 (fig. 2*A*). This waveform clearly demonstrates that the body wave and fundamental-order dispersive normal mode travel at nearly the same speeds, and the interpretation of the large amplitude waveform features such as S100-1 and S100-2 as the fundamental- and first-order DSNM appears to be sound.

The dominant frequencies of the fundamental- and first-order DSNM are very similar for the endcap set no. 1 waveforms (fig. 2*A*). This is not the case for the waveforms measured using endcap set no. 2, as shown in figure 3*A*. Two interpreted waveform features are shown as blue and red colors for the 150- and 200-mm-long cylinders. The dominant frequencies of the first part of the arrivals, shown in blue as S100-1, S150-1, and S200-1, range from 0.7 to 0.9 MHz, with the longer cylinder displaying a higher dominant frequency. The dominant frequencies of the second part of the arrivals, shown in red as S150-2 and S200-2, range from 0.28 to 0.4 MHz. As can be seen in figure 3*A*, the frequency content changes abruptly for S150-2 and S200-2 relative to S150-1 and S200-1. Figure 3*B* shows the measured group velocities along with the approximate group velocities calculated from $J_1(ma) = 0$ with $n = 0$ and $n = 1$. Contrary to the results using endcap no. 1, all of the measured group velocities for endcap no. 2 appear to follow the same trend as the calculated group velocities of fundamental-order DSNM.

Velocity Analysis

Relating the group velocity to the dominant frequency of a waveform feature using the approximated group velocity given by equation 12 appears to work well when identifying waveform features generated by endcap set no. 1 (fig. 2*B*). Normal mode identification is less obvious for features S150-2 and S200-2 when using endcap set no. 2 (fig. 3*B*), partly due to analyzing features with frequencies below 0.4 MHz using equation 12, which is intended for group velocities at high frequencies. Here we use the exact dispersion and group velocity equations (eq. 7 and 11) to investigate the possibility that the S150-2 and S200-2 features in figure 3 are combinations of the fundamental and first-order normal modes, rather than being purely first-order normal modes.

Figure 5*A* shows the exact and approximated phase and group velocities for the fundamental-order DSNM, whereas figure 5*B* shows the first-order DSNM. The symbols indicate the measured results taken from figures 2*B* and 3*B* and plotted for comparison with the theoretical curves. The black symbols are the fundamental-order normal-mode waveform features, whereas the white symbols are first-order normal-mode features. The split-color symbols are the waveform features that appear to be superposition of both the fundamental and first-order normal modes, as discussed below.

Figure 5 indicates that the approximated phase and group velocities derived from $J_1(ma) = 0$ appear to be appropriate for frequencies greater than about 0.4 MHz, both for the fundamental-order DSNM features identified in figure 5*A* and the first-order DSNM in figure 5*B,* because of similar trends. For frequencies less than about 0.4 MHz, the approximated group velocity diverges from the exact solution for the first-order DSNM (fig. 5*B*), indicating that the Bessel function approximation should not be utilized below 0.4 MHz. Therefore, the approximate group velocity curves shown in figure 3*B* or in figure 5 should not be expected to provide insight for the split-color features S150-2 and S200-2 measured using endcap set no. 2.

These group velocities shown by the split-color symbols fall reasonably close to the first-order group velocity predicted using the exact solution (fig. 5*B*) and can be characterized as first-order DSNM. Additional insight into these arrivals can be gained by examining their power spectra (fig. 6). Figure 6 compares the power spectra for S200-1 and S200-2 measured using endcap set no. 1 in figure 6*A* with those using endcap set no. 2 in figure 6*B*. The first characteristic observed in figure 6 is that the power spectra for the endcap set no. 2 data are complex relative to that of the first-order DSNM using endcap set no. 1. Also, S200-2 measured using endcap set no. 2, unlike the other features in figure 6*A*, has two prominent frequency components: one at 0.31 MHz and one at 0.525 MHz.

Figure 5*B* indicates that the measured group velocity of S200-2 measured using endcap set no. 2 at the lower dominant frequency, 0.31 MHz, agrees with the exact group velocity of the first-order DSNM. At the higher frequency component, 0.525 MHz, the measured group velocity agrees with the exact group velocity of the fundamental-order DSNM. This can be seen in figure 5*A* by shifting the split-colored symbol at 0.31 MHz across to 0.525 MHz, maintaining its plotted group velocity. Based on this agreement between the high-frequency component of S200-2 and the exact solution prediction of the fundamental-order DSNM group velocity, combined with the agreement between the low-frequency component and the exact solution prediction of the first-order DSNM group velocity, we conclude that S200-2 is a combination of the fundamental- and first-order normal modes. The same situation holds for S150-2, as measured by endcap set no. 2.

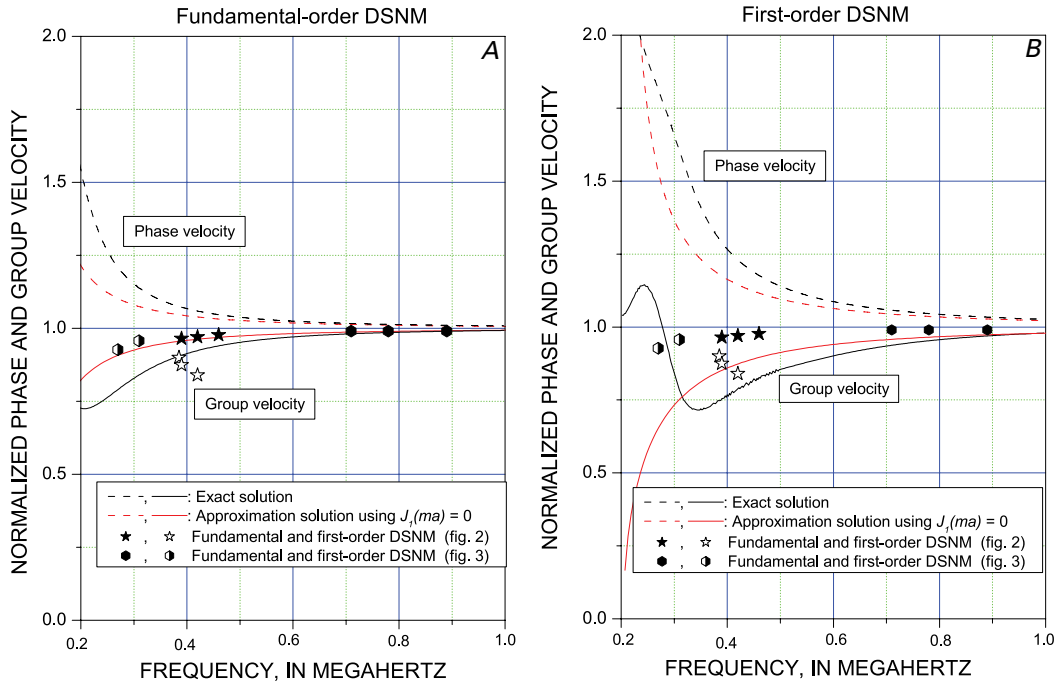

Figure 5. Exact and approximate normalized phase and group velocities. *A*, Fundamental order. *B*, First order. Measured group velocities of both orders are plotted in both *A* and *B* for comparison. Symbols are the same as for figures 2*B* and 3*B*, with fundamental modes as black symbols, the first-order normal modes as white symbols, and combined fundamental and first-order normal modes as split-color symbols. DSNM, dispersive shear wave normal mode.

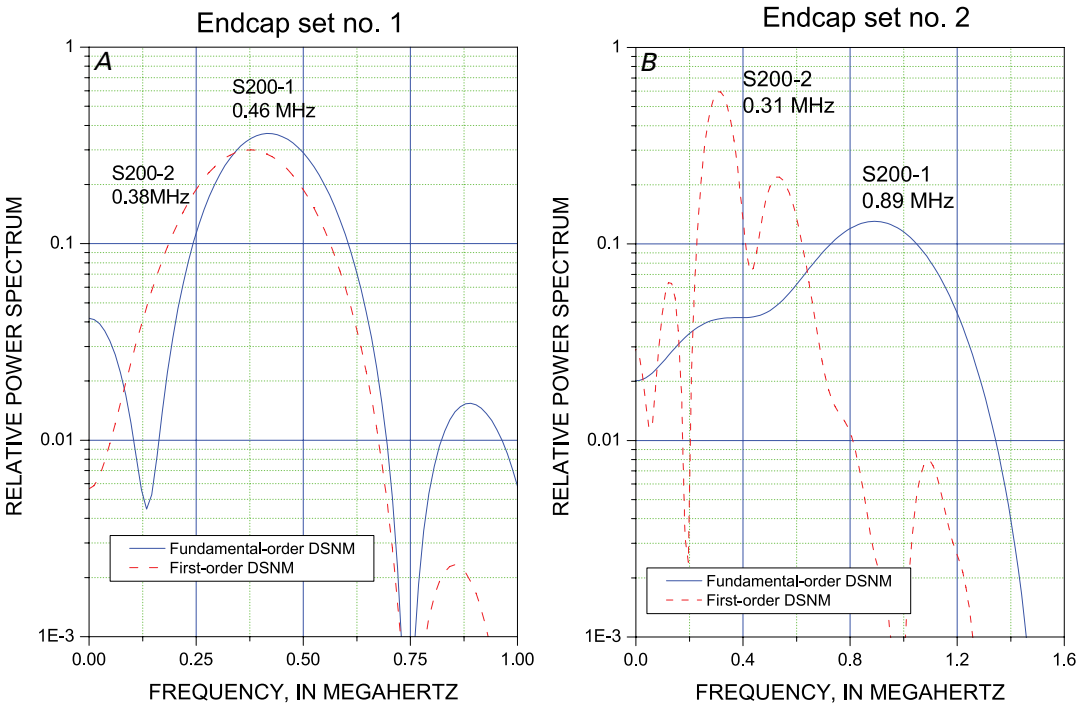

Figure 6. Measured power spectra for the 200-mm-long aluminum cylinder. *A*, Measured using endcap set no. 1, displaying a single dominant frequency for both the fundamental- and first-order DSNM. *B*, Measured using endcap set no. 2, displaying a single dominant frequency for the fundamental-order DSNM, but two significant frequency contributions for the first-order DSNM. DSNM, dispersive shear wave normal mode.

The mixture of two normal modes is not evident for the 100-mm-long aluminum cylinder. This kind of mixture of normal modes occurs because there exists a minimum group velocity. For example, this minimum group velocity occurs at approximately 0.34 MHz for the first-order normal mode (fig. 5*B*). Therefore, it is emphasized that the approximate group velocities derived from the Bessel function are valid only for high frequencies, meaning frequencies greater than the frequency corresponding to the minimum group velocity.

The mixture of normal modes is not seen in endcap set no. 1, for which the fundamental and first-order group velocities are distinct enough to produce distinct waveform features, as seen in figure 2*A*. These waveform features each have a single dominant frequency, as seen in figure 6*A*, indicating that they are not a superposition of two normal modes. However, the group velocities of S150-2 and S200-2 are between those of the fundamental- and the first-order normal modes, and as the frequency decreases, the group velocity agrees better with that of the fundamental order. At present, there are no satisfactory explanations for the abnormal group velocity behavior of S150-2 and S200-2, although bad resonance/vibration associated with the transmitted signal could have affected the analysis of the waveforms (D.R. Hutchinson, written commun., 2006). With this uncertainty, it is assumed hereafter that S150-2 and S200-2 measured using endcap set no. 1 are the first-order DSNM.

It is emphasized that the approximate group velocities derived from the Bessel function appear to be useful for frequencies greater than the frequency corresponding to the minimum group velocity. The frequency corresponding to the minimum group velocity increases as the order of normal mode increases. Therefore, it is more difficult to apply the approximate group velocity using the Bessel function when analyzing the higher-order normal modes.

Because of the existence of minimum group velocities for the DSNM discussed in this report, the application of waveform analysis using the approximate group velocities is limited. Consequently, the exact solution of the dispersion relation for DSNM should be used to accurately analyze measured waveforms. As opposed to the S-wave normal mode described in this report, however, the approximate phase (or group) velocities derived from $J_0(ma) = 0$ for torsional wave modes are very accurate, as shown in appendix 2. For torsional modes, either the exact or approximate phase (or group) velocity can be used and the accuracy of the approximated velocity increases as the normal mode order and frequency increase. Although the torsional wave is not the subject of this report, it is included, because the approximate dispersion relation of torsional wave is instructive for understanding various normal modes.

Amplitude Analysis

As an independent check on the normal-mode approach used to identify waveform features, we compared the predicted relative amplitudes of the waveform features. Figure 7 shows a comparison of the amplitudes of the fundamental and first-order DSNM calculated with both the exact dispersion relation and approximate dispersion relation using $J_1(ma) = 0$ with $n = 0$ and $n = 1$ for the 200-mm-long cylinder. The largest amplitude difference occurs near 0.3 MHz. The amplitude of the approximate solution is within about 30 percent of the exact amplitude for frequencies greater than 0.4 MHz for the fundamental-order DSNM. The amplitude of the first-order DSNM calculated using the approximation solution is remarkably close to the exact amplitude, within 10 percent of the exact solution, for frequencies greater than 0.4 MHz. Although the magnitude of the approximate solution is smaller than that of the exact solution for the fundamental-order DSNM, the amplitude trends with respect to frequency are similar, indicating that the approximate solution can be used to qualitatively compare the amplitudes of the different normal modes at high frequencies.

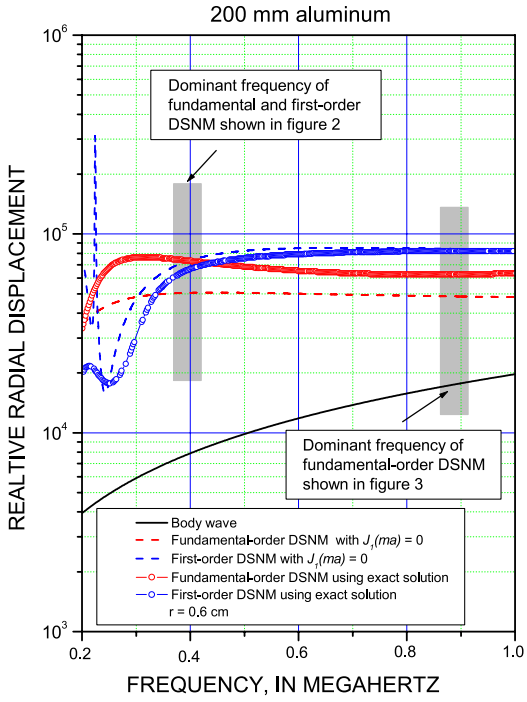

Figure 7. Calculated amplitudes for body wave and for fundamental- and first-order dispersive S-wave normal mode (DSNM) using the exact and the approximate dispersion relations.

Either the approximate or exact dispersion relation can be used to calculate the DSNM amplitudes at high frequencies. However, calculating the exact dispersion relation numerically is much more complicated than calculating the approximate relation. Therefore, it is more practical to utilize the approximate solutions for frequencies greater than the frequency of the minimum group velocity. When analyzing amplitude for frequencies less than or near frequencies of the minimum group velocity, however, the exact dispersion relation must be used.

The waveforms in figure 2*A*, measured using endcap set no. 1, have fundamental- and first-order normal modes that are of similar magnitudes. By comparison, the waveforms measured with endcap set no. 2 (fig. 3*A*) each have a fundamental mode that is larger than the trailing feature containing the first-order normal mode contribution. Because of their very different frequency content, separate analysis was required for the endcap no. 1 and endcap no. 2 results.

Two different frequency ranges are highlighted in figure 7 and are indicated by shaded boxes. The first shaded area in figure 7 spans the frequency range between 0.38 and 0.42 MHz and contains the dominant frequencies of the fundamental- and first-order normal modes for the 200-mm-long cylinder waveforms measured using endcaps no. 1 (fig. 6*A*). The amplitude of the fundamental-order DSNM at the dominant frequency of 0.42 MHz is comparable to that of the first-order DSNM at the dominant frequency of 0.38 MHz. As mentioned previously, the amplitude of the fundamental-order DSNM is mixed with the amplitude of body wave, which decreases at 1/length and is small compared to the normal mode amplitudes. Therefore, the normal-mode solution predicts that the amplitudes of the fundamental- and first-order DSNM are comparable and independent of the cylinder length. Measured waveforms shown in figure 2*A* support this prediction.

The second shaded area shown in figure 7 covers the frequency range spanned by the fundamental-order normal modes observed for 200-mm-long aluminum cylinder using endcap set no. 2 (S200-1). Note that the dominant frequencies for the S100-1, S150-1, and S200-1 waveform features are 0.71 MHz, 0.78 MHz, and 0.89 MHz, respectively. Because these frequencies are within the validity range for using the approximate solution, the normal mode amplitudes can be calculated using the approximate dispersion equation. Because the amplitude of the body wave at high frequencies is the same order of magnitude as the fundamental-order DSNM, the amplitude of the fundamental-order DSNM could have some contribution from the body wave.

The S150-2 and S200-2 waveform features are each a mixture of the first-order normal mode and the tail of the fundamental-order normal mode. The first-order normal mode amplitude near 0.3 MHz shown in figure 7 is relatively small compared to the fundamental mode. As indicated by the figure 3*A* waveforms, the amplitudes of the first features are indeed larger than the amplitudes of the second features. However, because the waveforms show constructive and destructive interference, interpreting the mixed waveform amplitudes using the theoretical amplitude relation shown in figure 7 requires caution.

Discussion

Phase Velocity and Normal Mode

The discontinuous phase and group velocities shown in figure 4 are caused by the assumption made to allow phase velocities to be greater than the S-wave velocity of the cylinder. There exist two different normal mode propagations, depending on the assumptions about phase velocity:

1. S-wave normal modes (described here) are derived assuming phase velocity cannot be less than shear wave velocity, and

2. extensional wave derived assuming that the high-frequency phase velocity can be less than the shear wave velocity (Kolsky, 1963).

As the frequency increases or wavelength decreases, the S-wave normal mode velocities shown in figure 4*A* approach the shear-wave velocity of the cylinder, whereas the shear and group velocity of an extensional wave or lowest axial-radial mode approaches that of the Rayleigh surface wave velocity of the cylinder, which is about 0.93β (fig. 8) (Thurston, 1978).

Two different normal mode propagations appear to be generated in the region indicated as “transition zone” in figure 4*A* when the wavelength is a little less than the cylinder radius. One mode develops into the fundamental-order DSNM (fig. 4) and one develops into the Rayleigh surface wave (fig. 8). The extensional wave propagation that develops into the Rayleigh surface wave is the well-known conventional longitudinal wave propagation (Kolsky, 1963; Graff, 1975; Thurston, 1978). However, it appears the fundamental S-wave normal modes described here are rarely observed or discussed. Except for the fundamental-order normal mode, the higher DSNM described in this report are the same as the higher-order extensional modes as long as the phase velocity is greater than the S-wave velocity and less than the P-wave velocity of the cylinder (Kolsky, 1963; Graff, 1975).

Cut-Off Frequencies

Equations 11 and 12 indicate there exists a cut-off frequency for each normal mode at which the phase velocity becomes infinite or the group velocity becomes zero. The exact cut-off frequency can be obtained from the dispersion relation by setting $k = 0$ (Thurston, 1978). Inserting $k = 0$ into equation 6, the cut-off frequency satisfies the following equation:

$$J_1(ma)[2\beta^2 lJ_1(la)/a - \omega^2 J_0(la)] = 0 \qquad (20)$$

For DSNM, the term in square brackets is never zero, meaning the cut-off frequency is given by the solution of $J_1(ma) = 0$.This is exactly the same assumption made for the deriving the approximate solution. Therefore, the cut

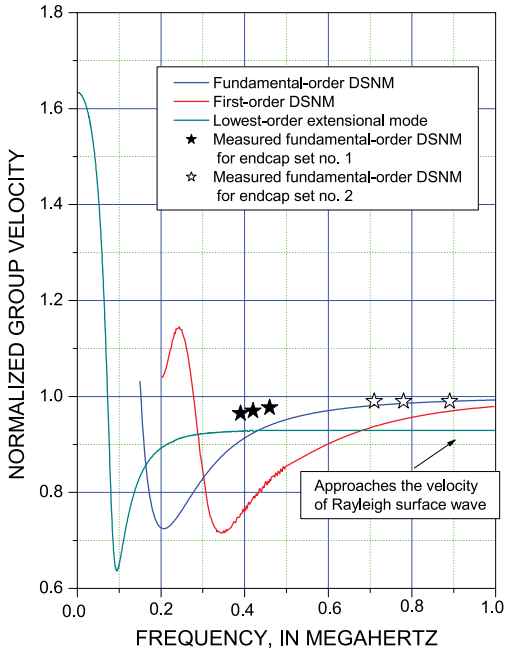

Figure 8. Calculated group velocity for fundamental (lowest)-order extensional mode, which was calculated under the assumption that the phase velocity changes continuously from greater than the shear-wave velocity to less than the shear-wave velocity, with those for the fundamental- and first-order DSNM. When the wavelength is small compared to the cylinder radius, the velocity of the fundamental extensional wave approaches the velocity of the Rayleigh surface wave, whereas the velocity of the fundamental-order DSNM approaches the shear wave velocity. DSNM, dispersive shear wave normal mode.

off-frequency at short wavelength is given by $\Lambda_\beta = \Pi_\beta$. For example, the cut-off frequency of the first-order DSNM is 0.20 MHz, when β = 3,180 m/s and a = 0.0175 m. The group velocity curve for the first-order DSNM shown in figure 8 (red curve) confirms this cut-off frequency. As the normal mode order increases, the cut-off frequency also increases.

Basis of Normal Mode Interpretation

The S100-1, S150-1, and S200-1 waveform features shown in figures 2 and 3 are interpreted as the fundamental-order DSNM, but there are other interpretations possible. These features could also be interpreted as shear body waves, Rayleigh surface waves, or second-order extensional waves. Based on the following arguments, however, these other interpretations cannot be valid, indicating that these features must be the fundamental-order DSNM. The reasons are as follows:

1. If these are S-body wave arrivals, their amplitude dependence on distance does not agree with the theory. Body wave amplitudes decay at 1/length, but the amplitudes of S100-1, S150-1 and S200-1 have almost the same amplitude even though the length of the S200-1 cylinder is almost twice that of S100-1.

2. If these are first-order extensional waves at high frequencies, otherwise known as Rayleigh surface waves, their group velocities are too slow. The observed fundamental-order normal mode features have group velocities exceeding 0.95β, whereas the surface Rayleigh wave velocity is about 0.93β, which is about 2,962 m/s (fig. 8, light blue curve).

3. If these are second-order extensional waves (Kolsky, 1963), their group velocities are too slow (fig. 8). The group velocity of the second-order extensional wave, which is the same as the first-order DSNM, is 3,056 m/s at 0.7 MHz, whereas the measured velocity for the S100-1 waveform feature measured at this frequency exceeds 3,180 m/s (fig. 3*B*). The velocity discrepancy becomes more pronounced as the frequency decreases (the first arrivals shown in figure 2).

Therefore, considering arrival times together with the amplitudes shown in figures 2 and 3, a logical interpretation of S100-1, S150-1 and S200-1 is that they are the fundamental-order S-wave normal modes described in this report.

Conclusions

Normal mode solutions in a cylindrical coordinate system qualitatively explain large amplitude arrivals measured for aluminum cylinders with various lengths. Those waveform features have amplitudes and arrival times that differ from the well-known shear body and bar waves. The following conclusions can be drawn from this investigation:

1. The phase and group velocities of the waveform features can be approximated using the Bessel function of the first kind for frequencies greater than the frequency corresponding to the minimum group velocity, which is about 0.4 MHz in this analysis. For frequencies less than 0.4 MHz, exact numerical solutions of the dispersion relation should be used to analyze measured waveforms.

2. The normal mode amplitudes calculated using the approximated dispersion relation ($J_1(ma) = 0$) are comparable to those calculated from the exact relation, and the qualitative analysis of the normal mode amplitude can be accomplished using the approximated solution at high frequencies.

3. Two remarkably different waveforms were observed depending on which endcaps were used in the investigation. Using endcap set no. 1, the fundamental-order dispersive S-wave normal mode (DSNM) and the first-order DSNM are observed as distinct arrivals, whereas using endcap set no. 2, single continuous waveforms with quite different frequencies were observed. Using endcap set no. 1, the amplitudes of the separate fundamental- and first-order DSNM are comparable for the 100-, 150- and 200-mm-long aluminum cylinders. Using

endcap set no. 2, it appears that the low-frequency part of the first-order DSNM and the high-frequency part of fundamental-order DSNM arrive at the same time, resulting in a waveform feature that is a superposition of low- and high-frequency energy. Detailed analyses of group velocity and relative amplitudes using the exact dispersion equation are required to fully understand the nature of these complex waveforms.

4. It is not clear why two distinct and remarkably different waveforms were measured using the two different endcaps, though the differing frequency content emitted from the two endcap sets is partly responsible for this difference. The observed differences highlight the importance of characterizing the transmitted signal using well-characterized samples, such as aluminum cylinders, prior to utilizing the waveform to characterize unknown material.

Acknowledgments

This work was supported by the Gas Hydrate Project within the U.S. Geological Survey's Energy Program and Coastal & Marine Geology Program. We thank Peter M. Bratton for his assistance in measuring acoustic waveforms and K. Lewis and W. Winters for many helpful comments and suggestions.

References Cited

Aki, Keiiti, and Richards, P.G., 1980, Quantitative Seismology—Theory and methods: New York, Freeman and Company, 932 p.

American Society for Testing and Materials, 2003, ASTM Standard D2850-03a Standard test method for unconsolidated-undrained triaxial compression test on cohesive solids, *in* Annual book of ASTM standards: West Conshohocken, Penn., ASTM International, p. 1−6.

Båth, Markus, 1968, Developments in solid earth geophysics: New York, Elsevier, 415 p.

Berge, L.I., Jacobsen, K.A., and Solstad, A., 1999, Measured acoustic wave velocities of R11 (CC13F) hydrate samples with and without sand as a function of hydrate concentration: Journal of Geophysical Research, v.104, p. 15415−15424.

Biot, M., 1952, Propagation of elastic waves in a cylindrical bore containing a fluid: Journal of Applied Physics, v. 23, p. 997−1009.

Brekhovskikh, L.M., 1960, Waves in layered media: New York, Academic Press, 559 p.

Dai, Jianchun, Snyder, F., Gillespie, D., Koesoemadinata, A., and Dutta, N., 2008, Exploration for gas hydrate in deep water, northern Gulf of Mexico—Part I. A seismic approach based on geologic model, inversion, and rock physics principle: Marine and Petroleum Geology, v. 25, p. 830−844.

Ewing, W.M., Jardetzky, W.S., and Press, F., 1957, Elastic waves in layered media: New York, McGraw-Hill, 380 p.

Graff, K.F., 1975, Wave motion in elastic solids: New York, Dover, 649 p.

Greenfield, R.J., 1978, Seismic radiation from a point source on the surface of a cylindrical cavity: Geophysics, v. 43, p. 1071−1982.

Helgerud, M.B., Dvorkin, J., Nur, A., Sakai, A., and Collett, T., 1999, Elastic-wave velocity in marine sediments with gas hydrates—Effective medium modeling: Geophysical Research Letters, v. 26, p. 2021−2024.

Kolsky, H., 1963, Stress waves in solids: New York, Dover, 213 p.

Lee, M.W., and Balch, A.H., 1982, Theoretical seismic wave propagation from a fluid-filled borehole: Geophysics, v. 47, p. 1308−1314.

Lee, M.W., and Collett, T.S., 2005, Assessments of gas hydrate concentrations estimated from sonic logs in the Mallik 5L-38 well, N. W. T., Canada, *in* Dallimore, S.R., and Collett, T.S., eds., Scientific result for Mallik 2002 gas hydrate production research well program, Mackenzie Delta, Northwest Territories, Canada: Geological Survey of Canada, Bulletin 585, 10 p.

Lee, M.W., and Waite, W.F., 2009, High frequency normal mode propagation in aluminum cylinders: U.S. Geological Survey Scientific Investigations Report 2009–5142, 16 p.

Morse, P.M., and Feshbach, H., 1953, Methods of theoretical physics—Part I: New York, McGraw-Hill, 998 p.

Pekeris, C.L., 1948, Theory of propagation of explosive sound in shallow water: The Geological Society of America Memoir 27, 117 p.

Priest, J.A., Best, A., and Clayton, C.R., 2005, A laboratory investigation into the seismic velocities of methane gas hydrate-bearing sand: Journal of Geophysical Research, v. 110, B04102, doi:10.1029/2004JB003259.

Santamarina, J.C., Klein, K.A., and Fam, M.A., 2001, Soils and waves—Particulate materials behavior, characterization and process monitoring: New York, Wiley, 488 p.

Sloan, E.D., and Koh, C.A., 2007, Clathrate hydrates of natural gases (3d ed.): Boca Raton, Fla., CRC Press, 721 p.

Thurston, R.N., 1978, Elastic waves in cylinders and clad cylinders: Journal of Acoustical Society of America, v. 64, p. 1−37.

Waite, W.F., Kneafsey, T.J., Winters, W.J., and Mason, D.H., 2008, Physical property changes in hydrate-bearing sediment due to depressurization and subsequent repressurization: Journal of Geophysical Research, v. 113, B07102, doi:10.1029/2007JB005351.

Waite, W.F., Winters, W.J., and Mason, D.H., 2004, Methane hydrate formation in partially water-saturated Ottawa sand: American Mineralogist, v. 89, p. 1202−1207.

Watson, C.N., 1966, A treatise on the theory of Bessel functions: Cambridge, University Press, 804 p.

White, J.E., 1965, Seismic waves-radiation, transmission, and attenuation: New York, McGraw-Hill, 302 p.

Winters, W.J., Dillon, W.P, Pecher, I.A., and Mason, D.H., 2000, GHASTLI—Determining physical properties of sediments containing natural and laboratory-formed gas hydrate, *in* Max, M.D., ed., Natural gas hydrate in oceanic and permafrost environments: Dordrecht, Netherlands, Kluwer Academic Publishers, p. 311−322.

Yun, T.S., Francisca, F.M., Santamarina, J.C., and Ruppel, C., 2005, Compressional and shear wave velocities in uncemented sediment containing gas hydrate: Geophysical Research Letters, v. 32, L10609, doi:10.1029/2005GL022607.

Appendix 1. Approximate Phase Velocity

In the main text, the approximate phase (or group) velocity is derived from $J_1(ma) = 0$. If $J_0(ma) = 0$ is used to derive the approximate phase velocity, the phase velocity at high frequencies is given by

$$C_\beta = \beta \sqrt{\frac{\omega^2 a^2}{\omega^2 a^2 - \beta^2 \Lambda_\beta^2}} \tag{1–1}$$

with $\Lambda_\beta = (3\pi/4 + n\pi)$ and $\Pi_\beta = a\omega/\beta$.

If the fundamental order is given by equation 1–1 with $n = 1$ instead of $n = 0$, the phase and group velocities using equation 1–1 are more accurate than those derived from $J_1(ma) = 0$ with $n = 0$. Figure 1–1*A* shows the phase and group velocity of the fundamental order shown in figure 5*A* using equation 1–1 with $n = 1$, and figure 1–1*B* shows the first order shown in figure 5*B* using equation 1–1 with $n = 2$. Overall those velocities derived from equation 1–1 with one order higher than those derived from equation 8 appear to more closely match the exact solution. However, the amplitudes of the normal modes calculated using equation 1–1 (shown in fig. 1–2) are less accurate than those calculated using equation 8 (shown in fig. 7). Relative to the exact phase velocity, the phase velocity approximation using $J_0(ma) = 0$ is slightly high, which appears to significantly affect the predicted amplitude. It is not clear why this is the case because, in contrast, the phase velocity approximation using $J_1(ma) = 0$ is slightly low and the predicted amplitudes are much more accurate. One drawback of using $J_1(ma) = 0$ as the approximate dispersion relation is that the cut-off frequency using this approximation does not agree with that of the exact equation. Both approximations are useful, however, as either can be used depending on the analysis objective. Because the amplitude of the normal mode appears to be more diagnostic for identifying normal-mode arrivals, the approximation using $J_0(ma) = 0$ is used in the main text.

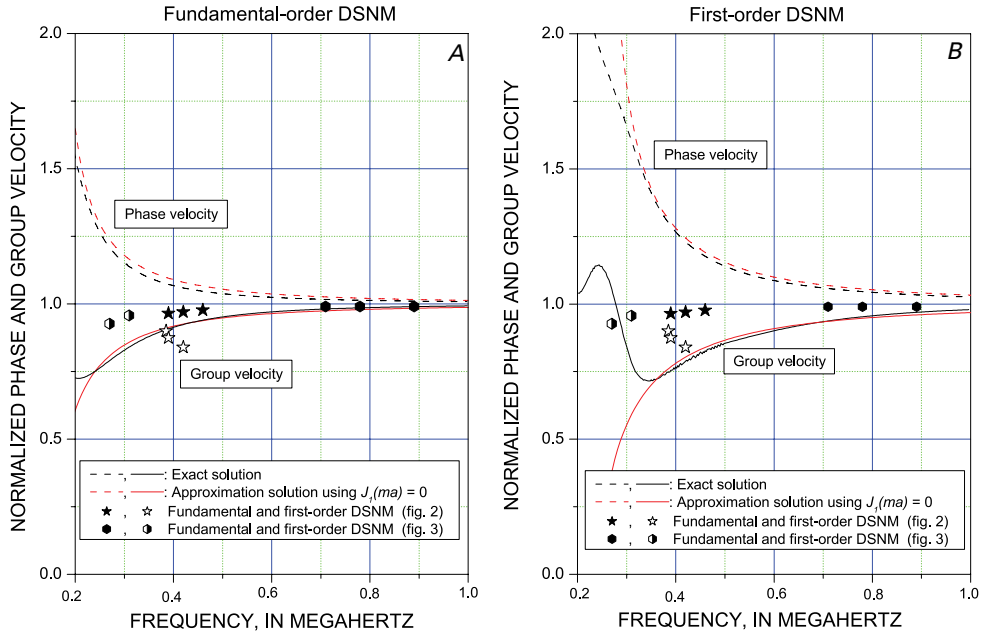

Figure 1–1. Exact and approximate normalized phase and group velocities using equation 1–1. *A*, Fundamental order. *B*, First order. Measured group velocities of both orders are plotted in both *A* and *B* for comparison. Symbols are the same as for figures 2*B* and 3*B*, with fundamental modes as black symbols, first-order normal modes as white symbols, and combined normal-and first-order modes as split-color symbols. DSNM, dispersive shear wave normal mode.

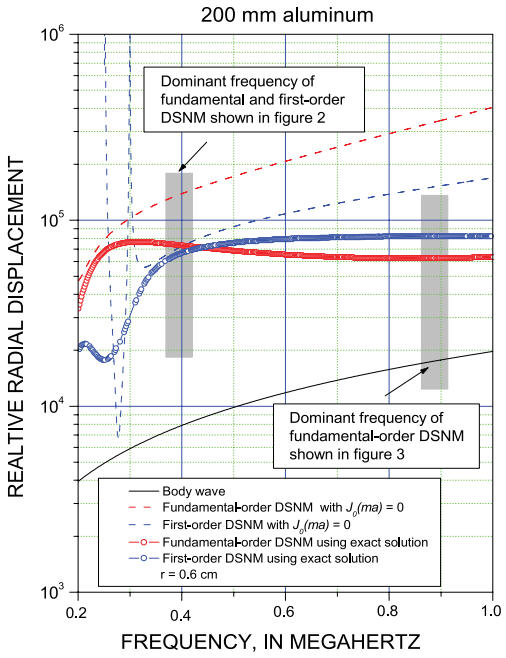

Figure 1–2. Calculated amplitudes for body wave and for fundamental- and first-order dispersive S-wave normal mode (DSNM) using the exact dispersion relation and the approximation shown in equation 1–1.

Appendix 2. Torsional Waves

In the torsional vibrations of a cylinder, each transverse section remains in its own plane and rotates about its center. The family of torsional modes results when only the azimuthal displacement is assumed to exist and is independent of the azimuthal angle. Therefore, the azimuthal displacement (U_θ) can be written as (Kolsky, 1963; Graff, 1975):

$$U_\theta = D\int J_1(mr)e^{-ikz}dk \tag{2–1}$$

The boundary condition for the torsional wave is $P_{r\theta} = \mu_1(\partial U_\theta / \partial r - U_\theta / r) = 0$ and the dispersion relation is satisfied by the following equation:

$$J_0(ma) = \frac{2J_1(ma)}{ma} \tag{2–2}$$

The solution of equation 2–2 can be numerically derived excluding $ma = 0$ (non-dispersive phase velocity). The first six solutions of equation 2–2 are $ma = 1.84093$, $ma = 5.33135$, $ma = 8.53623$, $ma = 11.70597$, $ma = 14.86357$, and $ma = 18.01549$. Therefore, the phase velocity of the torsional wave (C_T) is given by

$$\frac{C_T}{\beta} = \sqrt{\frac{a^2\omega^2}{a^2\omega^2 - \beta^2\hat{\Lambda}_\beta^2}} = \sqrt{\frac{1}{1 - \beta^2\hat{\Lambda}_\beta^2/(a^2\omega^2)}} \tag{2–3}$$

where $\hat{\Lambda}_\beta$ is the solution of equation 2–2, such as $ma = 1.84093$.

Equation 2–3 indicates that as the frequency increases, the phase velocity approaches the shear-wave velocity, and a cut-off frequency exists for each mode. The cut-off frequency (ω_c) is given by

$$\omega_c = \beta\widehat{\Lambda}_\beta / a. \tag{2–4}$$

The cut-off frequency increases as $\widehat{\Lambda}_\beta$ (or the order of normal mode) increases and as the diameter of the cylinder decreases.

If the dispersion equation is approximated using $J_0(ma) = 0$, the phase velocity is given by

$$\frac{C_T}{\beta} = \sqrt{\frac{a^2\omega^2}{a^2\omega^2 - \beta^2\Lambda_\beta^2}} = \sqrt{\frac{1}{1 - \beta^2\Lambda_\beta^2/(a^2\omega^2)}} \tag{2–5}$$

where $\Lambda_\beta = (3\pi/4 + n\pi)$. The difference between the exact and approximated phase velocities is in the difference between $\widehat{\Lambda}_\beta$ and Λ_β. The first six Λ_β are 2.355, 5.495, 8.635, 11.775, 14.925, and 18.055 (from $n = 0$ to $n = 5$). As the order of the normal mode (n) increases, the approximate phase velocity approaches the exact phase velocity. Calculated phase velocities using equations 2–3 and 2–5 are shown in figure 2–1. As shown in figure 2–1, the approximate phase velocity can be used for high-frequency normal-mode propagation for all orders of normal modes. Also, the approximate phase velocity can be used for normal mode propagation above that of the fundamental mode for all frequencies.

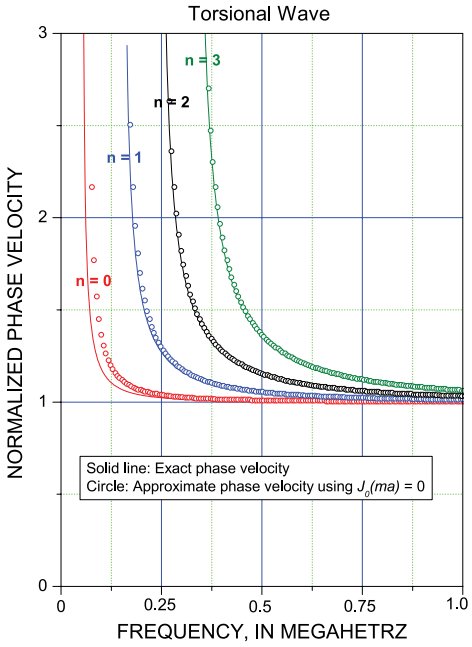

Figure 2–1. Calculated exact and approximate phase velocities for torsional waves for a 35-mm-diameter aluminum cylinder. The approximate phase velocities are derived from $J_0(ma) = 0$.

Publishing support provided by:
Denver Publishing Service Center

For more information concerning this publication, contact:
Team Chief Scientist, USGS Central Energy Resources
Box 25046, Mail Stop 939
Denver, CO 80225
(303) 236-1647